IET Science, Measurement & Technology

WILEY

The Institution of Engineering and Technology

ORIGINAL RESEARCH OPEN ACCESS

A New Box-Counting-Based-Image Fractal Dimension Estimation Method for Discharges Recognition on Polluted Insulator Model

Imene Ferrah[1] | Youcef Benmahamed[1] | Hayder K. Jahanger[2,3] | Madjid Teguar[1] | Omar Kherif[1,4]

[1]Laboratoire de Recherche en Electrotechnique, Ecole Nationale Polytechnique, Algiers, Algeria | [2]Department of Electronic and Electric Engineering, Swansea University, Swansea, UK | [3]School of Engineering, University of Warwick, Coventry, UK | [4]Advanced High Voltage Research Centre, Cardiff University, Cardiff, UK

Correspondence: Hayder K. Jahanger (hayder.jahanger@swansea.ac.uk)

Received: 8 August 2024 | **Revised:** 9 January 2025 | **Accepted:** 5 February 2025

Funding: The authors received no specific funding for this work.

ABSTRACT

This study presents an innovative approach to identify electrical discharges by proposing an algorithm incorporating fractal geometry concepts. Based on the box-counting method, our algorithm is developed to detect and track the progression of electrical discharges leading to flashover. This is achieved by calculating the fractal dimension of discharge images which are visual representations of electrical activity recorded during experiments on a planar glass insulator model subjected to different levels of contamination. First, the RGB image is transformed into a binary matrix using the NIBLAK binarization algorithm. Subsequently, the acquired matrix is converted into a square matrix, and its fractal dimension is computed for various resolutions. The final fractal dimension of the image is calculated using the least squares method. This latter is applied to the fractal dimensions (FDs) across all resolutions. According to our algorithm, discharge images have FD values ranging from 1.15 to 1.25. FD increases are observed with applied voltage and non-soluble deposit density (NSDD). The density and activity of discharges also increase with FD. Specifically, a discharge is considered “no-arc” if FD is less than 1.2 and “arc” otherwise.

1 | Introduction

High-voltage (HV) insulators are of critical importance in electrical transmission and distribution grids, as they are designed to function effectively even in the harshest climatic conditions. Consequently, monitoring the performance of these insulators, particularly under pollution, is of paramount importance to ensure the safe and continuous operation of the power grid [1–6].

To prevent flashover incidents and control the progression of electrical discharges, it is essential to develop dependable tools for real-time assessment of the performance of outdoor insulators [7, 8].

Monitoring insulator performance necessitates the prediction and forecasting of contamination severity [3, 5, 6, 8, 9]. Typically, this pollution assessment is conducted by investigating the leakage current (LC) [5, 10], or alternatively, through image analysis [1, 11, 12].

Several studies have focused on diagnosing polluted insulators by the (LC).

Chaou et al. [13] used recurrence quantification analysis (RQA) with eight indicators to analyse leakage current waveforms under different pollution levels. These indicators were applied to classification methods like KNN, Naïve Bayes, and SVM, showing a strong correlation between RQA indicators and pollution severity.

Similarly, Al Khafaf and El-Hag [14] developed a feed-forward neural network (FFNN) algorithm to predict and monitor fluctuations in the peak leakage current on polluted insulators, demonstrating significant correlations between peak leakage current changes and contamination levels.

In another study, Salem et al. [15] focused on the time-frequency characteristics of the leakage current to assess the condition of polluted polymeric insulators through laboratory tests on a 33 kV insulator string. They analysed temporal and frequency-domain indicators such as the curve slope index and crest factor, confirming their effectiveness in condition assessment.

Additionally, Salem et al. [16] introduced an index, Rh′, based on leakage current harmonics, to assess the risk of pollution on wet high-voltage glass insulators. They found that Rh′ outperformed the traditional 5th/3rd index in predicting flashover risk, particularly when the ratio of soluble to insoluble deposits was considered.

Gouda et al. [17] also contributed by developing a wireless device for monitoring high-voltage insulator contamination. The device continuously measures leakage current bursts, calculates the RMS value and sends alerts when a risk of power failure is detected. Tested in the laboratory, the device, powered by a solar bank, achieved an accuracy of 91.66% after 50 trials on insulators with different pollution levels. Together, these studies contribute to the advancement of insulator monitoring and flashover risk prediction using innovative techniques like RQA, neural networks, and harmonic analysis of leakage current.

In addition to leakage current-based methods, a recent study [18] introduces a probabilistic approach using the finite element method (FEM) to model insulator flashover and assess the failure risk under contamination. The voltage distribution along the insulator surface is estimated using FEM, while a random rotating urning wheel simulates the arc propagation. The flashover probability is determined for various contamination levels, and the Kolmogorov–Smirnov test is used to derive the contamination-based probability density function. The accuracy of the model is validated by comparison with the literature, and failure risk is calculated to predict transmission line outage rates.

However, beyond classical methods, fractal theory offers a powerful analytical tool for assessing the condition of polluted insulators by analysing the leakage current behavior [19–21].

Fractal analysis is a diagnostic technique for the real-time assessment and monitoring of insulator conditions. It is also used in image analysis and processing [22].

The theory of fractal geometry was introduced by Benoît Mandelbrot [23], who described it as a method to mathematically represent the irregular and fragmented shapes commonly observed in nature [23]. Unlike traditional Euclidean geometry, which deals with smooth and regular objects like lines, circles, and cubes, fractal geometry addresses complex, self-similar patterns that exhibit detail at every scale. Self-similarity means that a small part of the fractal structure resembles the whole, no matter how much you zoom in.

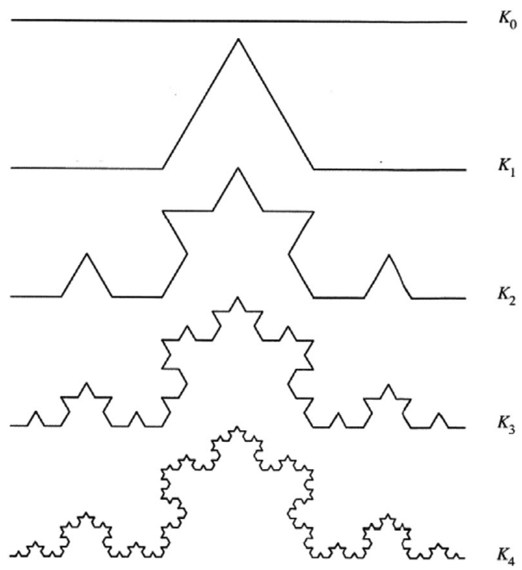

FIGURE 1 | The first stages of Koch's classical construction. All end points of the generated line segments are part of the final curve.

A fractal image is generally understood to be an image constructed in a recursive or self-similar manner. For instance, consider the branching patterns of blood vessels, tree branches, or even coastlines. These objects are considered fractal because their intricate structures exhibit high degree of similarity at different scales [23]. A well-known visual example of a fractal pattern is the Koch Curve [24] (see Figure 1), which reveals increasingly complex detail as it is magnified.

Fractal geometry has emerged as an efficacious and reliable analytical tool in various disciplines. In the field of electricity, fractal geometry is employed for modelling and analysing electric discharge phenomena [25]. The latter have an obvious fractal appearance [26]. Consequently, it can be defined by the fractal dimension. In reality, the electric discharge is multifractal [27]. Its shape transforms at each stage of its progression. This results in a fractal dimension that depends on the stage of progression. Consequently, in this study, the fractal dimension of the discharges at each stage of progression until total flashover is calculated.

The fractal dimension has been employed in numerous studies to analyse the dielectric breakdown phenomenon through the modelling of electric discharges. This results in simulated branched structures that are very different from real discharge shapes. Building on the foundation of fractal theory, its practical applications extend to optimize machining processes, as demonstrated by studies focusing on surface quality and morphology in electrical discharge machining techniques. To achieve improved surface quality through precise parameter adjustments using the fractal dimension, Mukhopadhyay et al. [28] integrated artificial neural networks (ANN) and genetic algorithms (GA) to optimize wire electrical discharge machining (WEDM) parameters. Their research focuses on discharge current, voltage, and pulse times, demonstrating how these adjustments effectively improve surface properties. Feng et al. [29] also utilized fractal theory to evaluate surface morphology in micro electrical discharge machining.

Sawada et al. [30] were the first to apply fractal theory to electric discharges, analysing the fractal properties of branched discharge structures in a stochastic model of dielectric breakdown. They introduced a key variable "R" that controls branch formation. However, they did not account for the local electric field, which caused discrepancies between simulated and real discharges. Two years later, Niemeyer et al. [31] improved the model by including the effect of the local electric field, demonstrating a correlation between discharge propagation and the field. Building on this, Wiesmann et al. [32] proposed a new fractal model of dielectric breakdown, called WZ.

Petrov et al [33] employed a fractal approach to quantify the probability of lightning strikes for modelled structures. Furthermore, the researchers considered the voltage drops that occur during the discharge.

In their study, Perera et al [34] used a stochastic dielectric breakdown model to simulate lightning discharges in both 2D and 3D domains. The authors evaluated the correlation between the fractal dimension of the discharge models and the value of the local electric field power, η. The fractal dimension of the simulated 3D discharge patterns and the 2D images of the lightning discharges were compared by taking projections of the simulated patterns. Additionally, the influence of ground objects on simulated lightning discharges was investigated.

Khelil et al [25] developed a fractal model describing the probability of lightning discharge interception of a grounded vertical rod when inserted in a rod-plane space. The height of the two grounded rods (representing a protective object and an object protected against lightning), their separation distance, and their location relative to the live rod were considered as parameters influencing the voltage and the breakdown time.

Four years later, they developed a fractal lightning protection model that considers the physical phenomena involved in the development of the electrical discharge [35]. The model incorporates the real physical conditions of discharge propagation, including downward and upward discharges from the protection system. It takes into account the voltage drop and the random nature of lightning discharges. The instantaneous breakdown voltage is estimated using both empirical equations and simulated discharge figures, with the model giving results in good agreement with experimental data.

To encompass the statistical nature of voltage breakdown in air for the coordinated insulation of transmission lines, Molas et al. [36] proposed a 3D fractal dimension calculation applied to a population of electrical discharges generated with a 3.4 MV lightning pulse and a 2.3 MV switching pulse under controlled laboratory conditions for sphere-sphere and sphere-plane electrode systems. The results demonstrate the ability of the method to effectively classify different types of discharges.

The novelty of this study lies in the application of fractal geometry to characterize images of electrical discharges, aiming to investigate the surface condition of a polluted insulator where these discharges occur. Our method is non-invasive, using highly detailed image analysis to avoid direct contact with the insulator, unlike techniques based on leakage current. It also allows for real-time monitoring of discharges and is sensitive to surface irregularities and subtle changes, offering improved detection of pollution variations by applying fractal analysis directly to RGB images. This integration of RGB imaging provides a more detailed and comprehensive assessment tool, complementing traditional methods. To this end, we have initially developed an algorithm for calculating the fractal dimension of images of electrical discharges evolving on a model of a polluted insulator. Specifically, an algorithm based on the box-counting method was implemented. The efficacy of the proposed algorithm was evaluated by applying it to the fractal curve of the Fibonacci word at a 90° angle, which has a well-documented fractal dimension. Furthermore, the algorithm was tested on the results obtained by Khelil [37]. These tests demonstrated the reliability of our algorithm. Subsequently, the fractal dimension of discharge images extracted from videos recorded during flashover tests on a flat insulator model subjected to pollution was calculated using the aforementioned algorithm. Finally, the influence of the applied voltage and the non-soluble deposit density (NSDD) on the fractal dimensions of the discharge images was studied, and the electrical discharges in the images were classified into two categories, "arc" and "no-arc," according to their fractal dimensions.

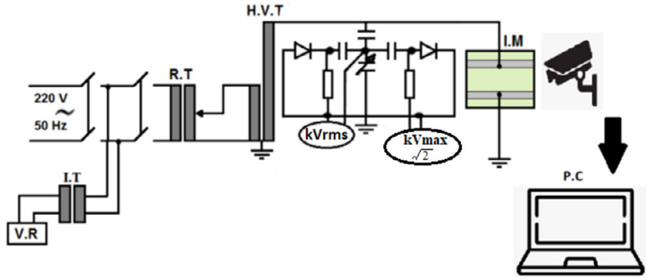

FIGURE 2 | Laboratory test arrangement. H.V.T indicates high voltage transformer; R.T, regulating transformer; I.T, isolating transformer; V.R, voltage regulator; I.M, insulator model; P.C, personal computer.

2 | Experimental Setup

Experiments were conducted at the High Voltage Laboratory of ENP (Ecole Nationale Polytechnique) using a flat insulator model that was exposed to uniform pollution. The experimental apparatus comprises a high-voltage test transformer (300 kV/50 kVA, 50 Hz), powered by a voltage regulator (220/500 V, 50 kVA, 50 Hz), a capacitive divider (with a 1000:1 ratio), and a model of a plan glass insulator of 50 cm by 50 cm by 5 mm (Figure 2). Two rectangular aluminium electrodes (50 mm by 3 cm by 2 μm) were employed, with a separation distance of 29.2 cm. This distance corresponds to the leakage path of the 1512L cap and pin outdoor insulator, which is primarily utilized by the Algerian Company of Gas and Electric Power (SONELGAZ). The insulator model (Figure 3) is positioned on a wooden support at a height of 100 cm from the ground (Figure 4). At the same height as the insulator model, a video camera (Full HD, 20 Megapixels) is employed to

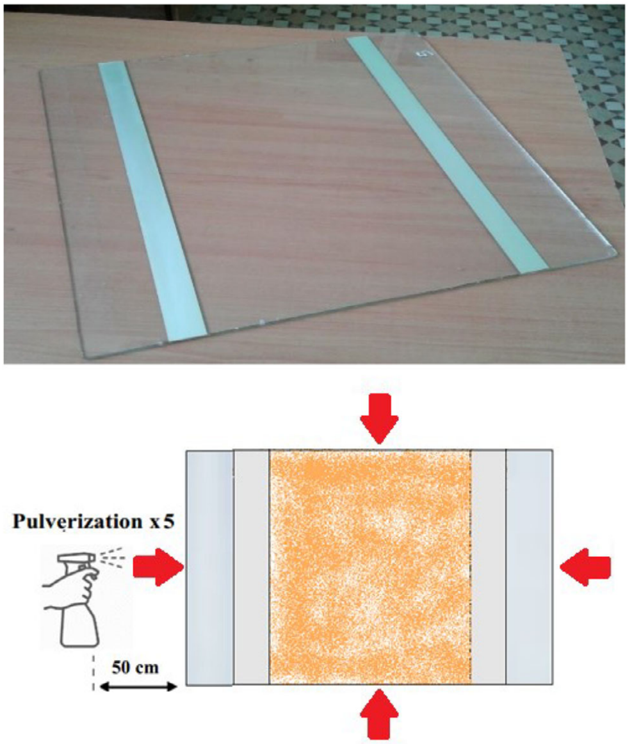

FIGURE 3 | Laboratory plane model profile [38] and schematic illustration of the pollution application process.

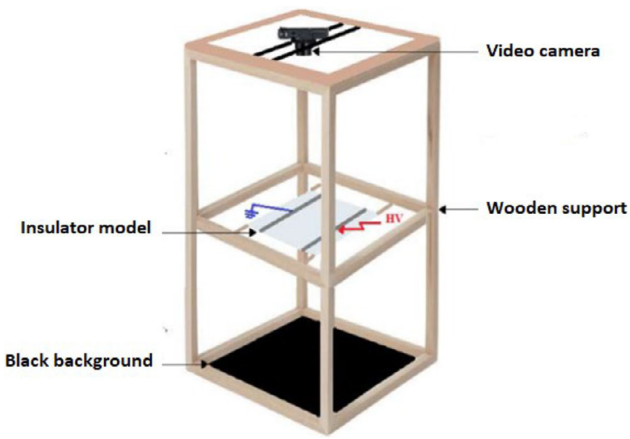

FIGURE 4 | Disposition of insulator model and video camera [12].

capture the evolution of discharges until flashover. Subsequently, the recorded data were processed on a personal computer (PC).

Before each test, the insulating surface is subjected to an initial cleaning process with tap water, followed by a drying phase. Subsequently, the surface is further cleaned with isopropyl alcohol in order to eliminate any traces of pollution. The insulator model is then subjected to uniform pollution utilizing sand collected from Naama City (southern Algeria) at a height of 20 m. To take into account the impact of the sand quantity on the insulator model, we considered four different amounts (15, 30, 45, and 60 g), corresponding to NSDD values of 0.01, 0.02, 0.03, and 0.04 g/cm^2, respectively. A highly accurate electronic scale was used to measure these quantities accurately. The NSDD values are calculated according to IEC 60815 [39]. The formula for NSDD is expressed as follows:

$$\mathrm{NSDD} = \frac{W_s}{A} \tag{1}$$

Here, A represents the surface area of the polluted insulator model in square centimetre and W_s the weight of the sand amount in grams.

The sand is manually spread on the experimental model using a sieve. The sand layers were moistened with distilled water (conductivity of 2 μS/cm measured with a conductivity meter) using a 20 mL sprayer, applied five times at a consistent distance of 50 cm from each side of the insulator model (Figure 3). Each test for a given NSDD value was repeated five times to ensure accuracy.

3 | Statistical Analysis of the Correlation Between Fractal Dimension, Voltage, and NSDD: Confidence Intervals and Analysis of Variance (ANOVA)

In this section, we introduce the statistical method of confidence intervals (CIs) [40] calculation to strengthen the reliability of our findings on the correlation between fractal dimension, applied voltage, and the NSDD on polluted insulators. The use of CIs provides an interval within which the true parameter value of a parameter (such as the slope of a regression model [41]) is expected to fall with a specified level of confidence. For our study, we compute 95% [40] confidence intervals to quantify the precision of our estimates and to assess the statistical significance of the observed relationships.

To investigate the relationship between fractal dimension, applied voltage (V) and the NSDD, we first perform a multiple linear regression analysis. The regression model can be written as follows [41]:

$$\mathrm{FD} = \beta_0 + \beta_1 \mathrm{V} + \beta_2 \mathrm{NSDD} + \epsilon \tag{2}$$

Here β_0 is the intercept, β_1 is the regression coefficient for voltage, β_2 is the regression coefficient for NSDD and ϵ is the error term.

The regression coefficients β_1 and β_2 represent the effect of voltage and NSDD on the fractal dimension, respectively. To determine the precision of these estimates, we calculate the 95% confidence intervals for β_1 and β_2.

The formula for a confidence interval for a regression coefficient β_i is [41]:

$$CI = \hat{\beta}_i \pm t_{\alpha/2,df} \times SE\left(\hat{\beta}_i\right) \tag{3}$$

where $\hat{\beta}_i$ is the estimated regression coefficient, $t_{\alpha/2,df}$ is the critical value from the t-distribution with df degrees of freedom at a 95% confidence level and SE($\hat{\beta}_i$) is the standard error of the estimated coefficient.

By calculating the confidence intervals for both β_1 and β_2, we assess whether the intervals contain zero. If the interval does not

TABLE 1 | Confidence Interval calculation results for voltage and NSDD about FD.

	Voltage	NSDD
Intercept β_0	−218.2618	−0.3051
Slope β_i	220.4222	0.2793
Intercept CI	[−237.1685, −199.3551]	[−0.3760, −0.2342]
Slope CI	[204.5962, 236.2482]	[0.2202, 0.3384]
R-squared	0.9781	0.8375

contain zero, it indicates that the corresponding variable has a statistically significant impact on the fractal dimension.

MATLAB (version 9.3.0) was used to calculate the confidence intervals (CI) for the relationship between the fractal dimension, applied voltage, and the NSDD. Linear regression analysis was conducted using the regress function. The tinv function was used to calculate the 95% confidence intervals for the regression coefficients. The standard errors of the coefficients β_0, β_1 *and* β_2 were calculated using the variance-covariance matrix.

The input data for this analysis comprises three vectors: applied voltage (V), fractal dimension (FD), and NSDD. Each vector contains N data points ($N = 21$), ensuring that all vectors are of equal length for consistency in the regression analysis. The vectors represent measurements taken under various experimental conditions (Section 2) to capture the relationship between FD, V, and NSDD. The results of the confidence interval calculations for the FD, the applied voltage and the NSDD are summarized in Table 1.

The results for the voltage indicate a strong and statistically significant positive relationship between the FD and the applied voltage. The slope coefficient of 220.4222 suggests that for each unit increase in FD, the applied voltage increases by approximately 220.42 units, highlighting the significant influence of FD on voltage. The 95% confidence interval for the slope, ranging from 204.5962 to 236.2482, further confirms the reliability of this relationship as the interval does not include zero, ensuring statistical significance. In addition, the R-squared value of 0.97813 indicates that 97.81% of the variation in applied voltage can be explained by the fractal dimension, leaving only 2.19% attributed to other factors or random variation.

The results for the NSDD indicate a statistically significant positive linear relationship between the FD and the NSDD, with a slope coefficient of 0.2793. This means that for each unit increase in FD, the NSDD increases by approximately 0.2793 units. The 95% confidence interval for the slope ranges from 0.2202 to 0.3384, confirming that the relationship is reliable and not due to random variation, as the interval does not include zero. The model's R-squared value of 0.83752 suggests that approximately 83.75% of the variation in NSDD can be explained by the variation in FD, indicating a strong relationship between these two variables. Notably, the negative intercepts for both voltage and NSDD reflect the estimated values when the fractal dimension is zero, which, though not physically meaningful, are essential for defining the linear models, with their narrow confidence intervals confirming the precision and statistical significance of the estimates.

Overall, the results obtained from the confidence interval calculations show a clear correlation between the FD, applied voltage, and NSDD.

In addition to using confidence intervals to analyse the relationship between the fractal dimension (FD) of the discharge images, the applied voltage, and the degree of pollution (NSDD), we utilized Analysis of Variance (ANOVA) [42]. This statistical method determines whether variations in the FD are significantly influenced by different levels of voltage or NSDD by comparing the variance between group means and within groups. Unlike confidence intervals, which estimate the precision of relationships, ANOVA directly tests the impact of these factors, thereby strengthening the conclusions of our study. ANOVA was applied to test the hypothesis that changes in the applied voltage or NSDD levels significantly influence the fractal dimension of discharge images. The null hypothesis (H_0) and the alternative hypothesis (H_1) are stated as follows:

- H_0: The means of the fractal dimension across different voltage or NSDD levels are equal (no significant effect).
- H_1: At least one group mean is different (a significant effect exists).

The ANOVA test statistic, F, is calculated using the formula [42]:

$$F = \frac{MSB}{MSW} = \frac{\frac{SSB}{k-1}}{\frac{SSW}{N-k}} = \frac{SSB\,(N-k)}{SSW\,(k-1)} \qquad (4)$$

where:

- MSB (mean square between): Represents the variability between group means.
- MSW (mean square within): Represents the variability within each group.
- SSB: Sum of squares between groups
- SSW: Sum of squares within groups
- k: Number of groups
- N: Total number of observations

The decision to reject or accept the null hypothesis is based on the calculated F-statistic and its corresponding p-value, which is a statistical measure used to determine the significance of results, indicating the probability of observing the data assuming the null hypothesis is true [42]. If the p-value is less than the chosen significance level $\alpha = 0.05$ [43], the null hypothesis is rejected, indicating that the means are significantly different.

In our case, the fractal dimension (FD) is the dependent variable while the applied voltage levels and the NSDD levels are the independent categorical variables.

By applying ANOVA, we aim to quantify the influence of voltage and NSDD on the fractal dimension values and determine

TABLE 2 | ANOVA results for NSDD and voltage effects on fractal dimension.

Source	Sum of squares	Degree of freedom	Mean Square	*F*-statistics	*p*-values
NSDD	14.6875	2	7.3437	445.1779	1.6902e-10
Voltage	2.1476	5	0.4295	26.0372	1.9765e-05
Error term	0.1650	10	0.0165	/	/
Total variance	17.0000	17	/	/	/

TABLE 3 | Typical discharge evolution until flashover [12].

Step	Typical discharge phenomena
1	No obvious arc discharge at 14.2 s (Figure 4a)
2	Weak spark at 15.5 s (Figure 4b)
3	Discharge in the shape of brushes at 15.9 s (Figure 4c)
4	Short local arc discharge at 16.3 s (Figure 4d)
5	Dense small arc discharge at 17 s (Figure 4e)
6	Bright main arc discharge 17.2 s (Figure 4f)
7	Intensive main arc discharge at 17.8 s (Figure 4g)
8	First and final arc flashover stages at 18 s (Figure 4h,i)

whether significant differences exist between these levels. This complements the confidence interval analysis previously conducted and provides additional statistical evidence for the observed relationships. A two-way analysis of variance (ANOVA) was performed using MATLAB (version 9.3.0). The analysis yielded an ANOVA table (Table 2), summarizing key parameters such as the sum of squares, degrees of freedom, mean square values, *F*-statistics, and *p*-values for each factor. The results indicated that NSDD has a highly significant effect on the fractal dimension (FD), as evidenced by the very small *p*-value (1.69×10^{-10}), which indicates a strong relationship between NSDD levels and FD. Voltage also has a statistically significant effect on FD, though its impact is smaller compared to NSDD, as reflected in the *p*-value (1.98×10^{-5}) and the sum of squares. The error term is small, suggesting that most of the variance in FD can be explained by NSDD and voltage.

The results of the ANOVA, including the *F*-statistic and *p*-values presented in Table 2, confirm that ANOVA revealed strong correlations between the fractal dimension (FD), applied voltage, and NSDD, highlighting significant interactions and dependencies between these variables.

4 | Flashover Stages

Previous studies [1, 9, 12] have focused on the evolution of discharges from their inception to flashover. Chaou et al [1] opted for two categories namely arcing and non-arcing. In this investigation, we adopted the same eight stages or typical discharges that characterize the flashover as considered in an earlier study [12]. Indeed, we present in Figure 5 and Table 3 the flashover process of the experimental model under NSDD pollution of 0.02 g/cm^2.

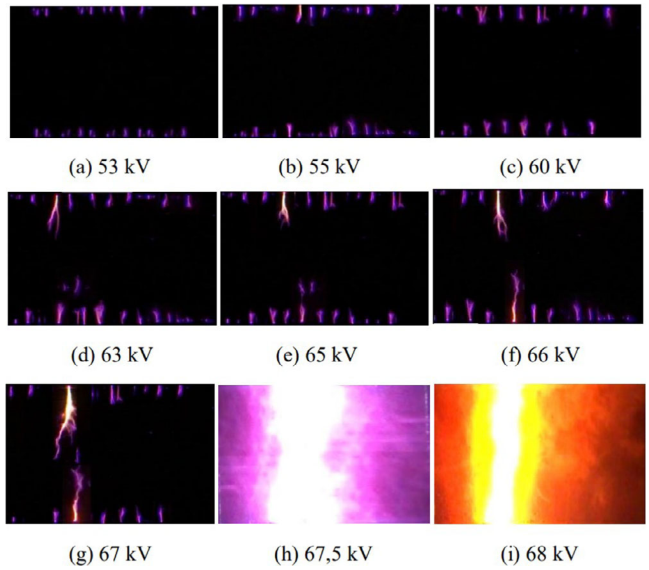

FIGURE 5 | Stages of flashover process [12].

At about 25 kV, the first luminosities appear on both sides of the insulator model electrodes. At about 50 kV, these luminosities become more apparent, and at 53 kV they develop into scattered bright spots (Figure 5a). These spots begin to coalesce into weak sparks as the applied voltage is increased to 55 kV (Figure 5b). At 60 kV, the sparks grow into brush discharges (Figure 5c). At 63 kV, the arc structure, consisting of tiny partial arcs, begins to appear (Figure 5d). It is important to note that the arcs generated so far are not regional.

A new phase describing the discharge evolution process is observed starting at 65 kV. During this phase, some arcs begin to fade. Conversely, two small arcs form on either side of the electrodes. Compared to the high voltage side, the arc on the ground side is longer. Denser and brighter arcs remain (Figure 5e). The length of the localized arcs increases and the total number of arcs decreases slightly after 66 kV (Figure 5f). The localized arcs become longer, denser, and thicker at 67 kV, eventually producing main arcs (Figure 5g). Flashover begins at 67.5 kV and occurs after the two arcs make contact, as shown in Figure 5h,i, which represent the first and last stages of flashover, respectively. The thickness of the flashover decreases from the initial to the final phase of the flashover. It is noteworthy that for each value of NSDD, the flashover process is identical to that described above.

5 | Binarization Results on Some Discharge Images

In this section, the main techniques of image segmentation by simple thresholding are compared by applying them to discharge images presented in Figure 5. This study allows selecting the thresholding algorithm to be adopted for our investigation.

Camera images are typically colour images. A colour image consists of three layers: red, blue, and green (RBG) [44].

Grayscale is a range of monochromatic shades from black to white. Therefore, a grayscale image contains only shades of Gray and no colour. Images commonly referred to as "black and white" in everyday language are called grayscale images in the digital image domain. An image with only two grayscale levels: 0 (black) and 1 (white) is called a binary image [45].

Simple thresholding segmentation methods (binarization), which are sensitive to noise, convert a grayscale image into a binary image based on the intensities of the pixels that make up the image to classify it into a particular category. If a pixel has a value within a certain threshold range, it is assigned a value of one; otherwise, it is assigned a value of zero, where S1 and S2 represent the upper and lower limits of the threshold range. Often, only S1 is given, assuming that S2 is the highest intensity value in the image. These techniques allow binarization of the image but with a loss of information. These losses do not have a significant impact on the images used, as they retain their main aspects [46].

There are global and local thresholding methods. Global thresholding ones apply a single intensity threshold to the entire image to separate it into two classes (background and object). The most common global thresholding methods include the Otsu method [47] and the Isodata method [48].

When the distribution of grayscale levels in an image is almost non-uniform, distinguishing between the background and the object of the image cannot be achieved with a single global threshold. It is necessary to consider the grayscale level of each pixel by assigning it a specific threshold based on the content in its vicinity. This is the principle behind local binarization methods. Among the most common local methods are those of Bernsen [49] and Niblack [50].

Table 4 summarizes the results of binarizing four discharge images using the segmentation methods mentioned above. The Brensen and Niblack methods were evaluated for window sizes of 15×15 and 25×25, respectively.

The results of these four methods were compared. Based on visual criteria, the Niblack algorithm appears to outperform the other methods in terms of thresholded image quality and information preservation. After a thorough visual examination of the experimental results, the main observations are summarized below:

TABLE 4 | Binarization results of discharge images using segmentation methods of Otsu, Isodata, Bernsen and Niblack.

Test images	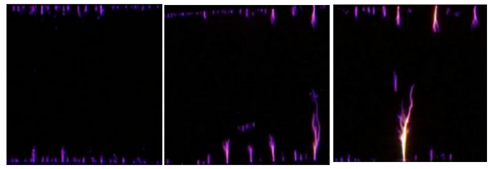
Otsu	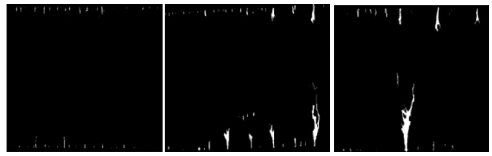
Isodata	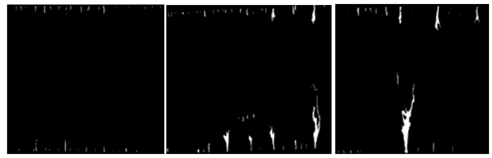
Bernsen	
Niblack	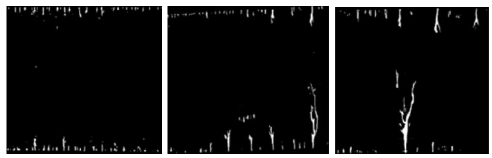

- ➢ The Otsu and Isodata methods show their effectiveness for discharge images. However, these two methods did not produce truly sharp binary images, for the simple reason that some background pixels were assigned to the object. Given that each background pixel should take 0, and each object pixel should take 1.
- ➢ With the Brensen approach, the resulting binary image usually contains a significant amount of background noise, especially in the background areas.
- ➢ The Niblack method solves the problem of background noise that occurs in the Brensen method. This method shows better performance than the other tested methods and works better especially when the images have extremely small intensity variations. For this reason, we have chosen to use the Niblack method for image binarization.

6 | Algorithm for Fractal Dimension Computation With the Box-Counting Approach

This section describes the development of an algorithm based on the box-counting method to calculate the fractal dimension. The algorithm was applied to discharge images extracted from videos recorded during tests on a high-voltage insulator model. The validation of our algorithm was performed using numerically modelled discharge images by [37] as well as the fractal dimension of the Fibonacci word, which has a known fractal dimension.

Among the techniques discussed by Mandelbrot [23], the box-counting method is recognized as the most suitable for fractal dimension (FD) estimation [51], due to its simplicity and effectiveness for studying temporal signals [52] and images [53, 54]. The box-counting method is based on the concept of "covering" the image with a rectangular coordinate grid (box). The number of these boxes is counted to determine how many are required to completely cover the active elements in the image under study. It widely regarded as the most effective technique for estimating FD [54]. For this reason, the box-counting method (BC) is one of the most commonly used techniques [55, 56].

In this section, we developed an algorithm in the MATLAB environment (version 9.3.0) to calculate the fractal Dimension (FD) of discharge images using the box-counting method. This algorithm is based on counting the number of boxes needed to completely cover the discharges in the image, calculating the FD at multiple resolutions. The FD of the image is typically estimated by the least squares method or by its average value across all resolutions.

Firstly, we consider a colour image coded in RGB of dimension Di*3 (Di being the initial dimension of the image to be processed). Next, we cover the entire image with boxes of the same size e (resolution). Then we count the number of active boxes N(e), that is, the number of boxes needed to cover the discharges in the image. Finally, the FD of the image is computed using Equation (5) [57].

$$FD_{bc} = \lim_{n \to \infty} \frac{\log (N(e))}{\log (1/e)} \tag{5}$$

The various steps taken during the design of the developed algorithm are summarised in the flowchart presented in Figure 6. To understand the process of calculating the fractal dimension using this algorithm, the flowchart is followed by a detailed explanation of its steps.

The flowchart in Figure 6 follows the steps outlined below:

a. We acquire the (RGB) image of the discharge with dimensions D_i*3, which will be the subject of the FD calculation.

b. We convert the RGB image into a grayscale image of dimension D_i, where the only colours are shades of Gray. This conversion is done by calculating the luminance value of each pixel, which is a weighted sum of the RGB values, this step simplifies the image by removing colour information while preserving intensity variations, which are crucial for further analysis.

c. We transform the resulting grayscale image into black and white because the box-counting algorithm we developed requires a binary input image. This involves segmentation, where we used the Niblack segmentation method (detailed in Section 5). At the end of this step, the image is represented by a binary matrix of dimension D_i, where each element is either 1 or 0, corresponding to the segmented regions of interest and background.

d. We fill the matrix with background elements to make it square and have its dimension as a power of 2 ($D^0 = 2^{n^\circ} * 2^{n^\circ}$)

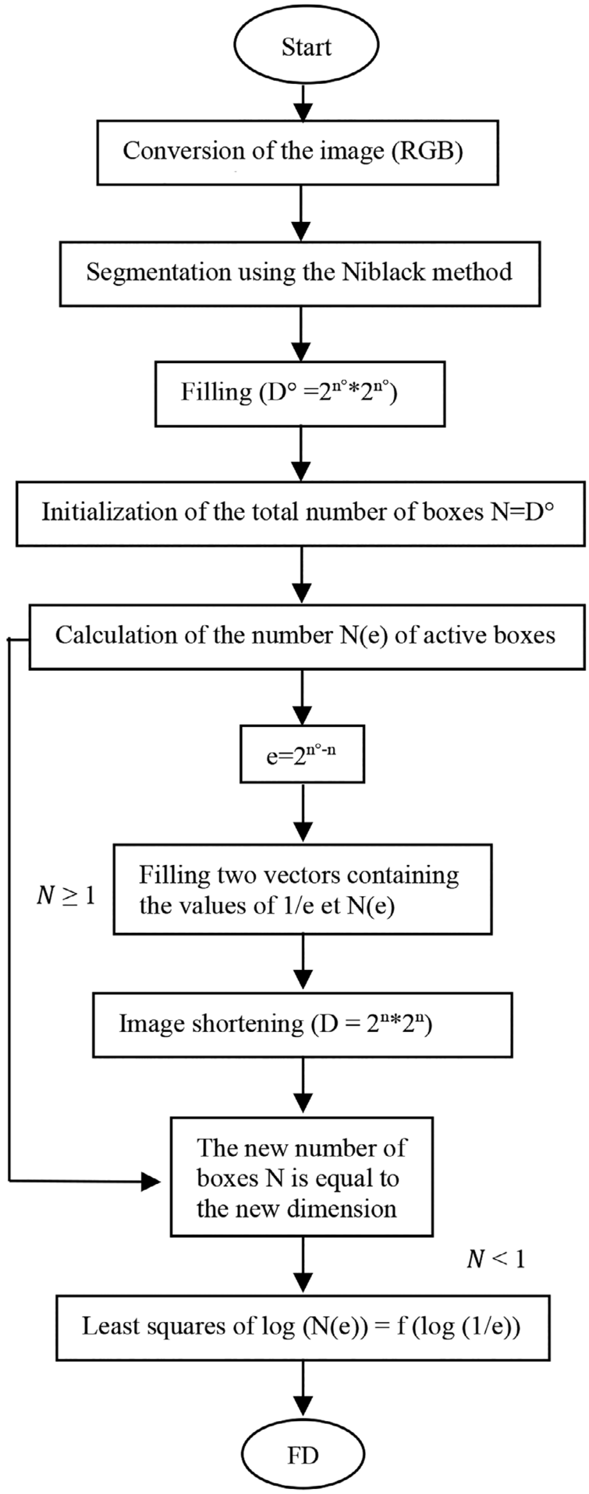

FIGURE 6 | Flowchart of the proposed box-counting algorithm.

(2^{n° represents the number of rows/columns of the obtained square matrix). An illustrative example of this operation is explained in Figure 7.

e. We initialize the total number N of boxes to the size of the matrix as the first resolution. This step involves dividing the binary matrix into smaller, equally sized square boxes, where each box covers an area of dimension e x e (where **e** is the box size). At this initial resolution, the box size e is set to 1,

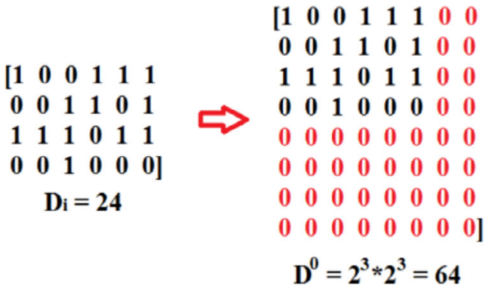

FIGURE 7 | Example of filling the background of a matrix with dimensions 24.

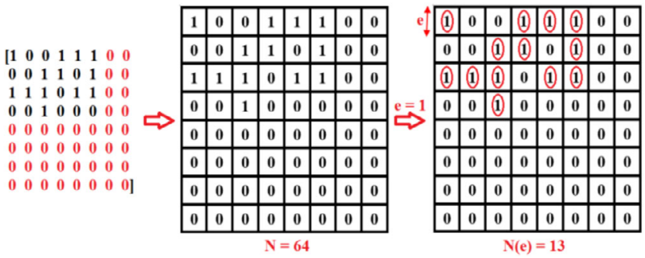

FIGURE 8 | Example of calculating the number of active boxes.

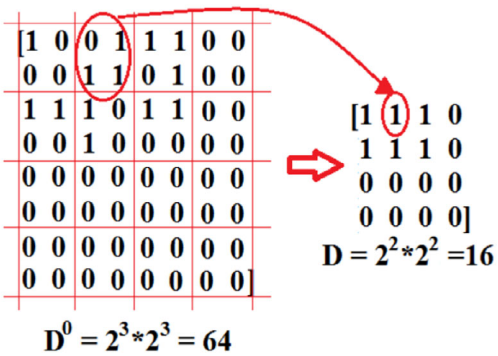

FIGURE 9 | Illustration of a shortened matrix using the logical summation of its elements.

meaning that each pixel is treated as an individual box and we calculate the number of active boxes N(e) which refers to the boxes containing at least one pixel with a value of 1. Figure 8 illustrates this step.

f. The FD for each resolution is given by the formula:

$$FD = \frac{\log(N(e))}{\log(1/e)} \tag{6}$$

At each iteration, we shorten the matrix from Figure 9. This gives us new values of e and N(e). Thus, we form vectors from the recorded values of 1/e and N(e) once all iterations are completed.

g. Now, we consider the shortened matrix as a new resolution, where the box dimension e is given by the formula: $e = 2^{n^{\circ} - n}$. This step marks the progression of the algorithm to a coarser resolution, where larger boxes are used to cover the matrix. By enlarging the box size, we aim to capture the global structure of the fractal pattern at multiple scales. The same aforementioned steps are repeated at this new resolution. This iterative procedure continues, with the resolution becoming progressively coarser, until the size of the shortened matrix is strictly less than 1, meaning no more subdivisions are possible. Through this multi-resolution analysis, the algorithm systematically measures the fractal dimension across different scales.

h. Eventually, we obtain two vectors containing the values of N(e) and e for all resolutions. Using the least squares method, we calculate the slope of Equation (5). This slope represents the fractal dimension of the image.

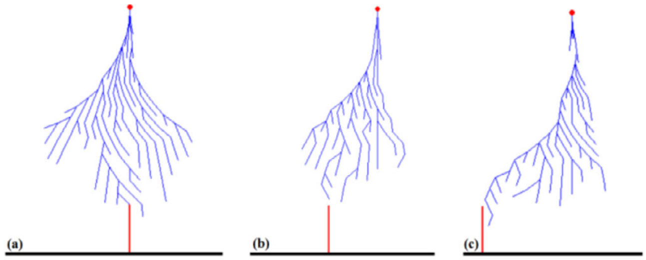

FIGURE 10 | Discharge shapes: (a) for $x = 0$ cm and $h = 2$ cm; (b) for $x = 2$ cm and $h = 2$ cm; (c) for $x = 3.7$ cm and $h = 2$ cm [37].

7 | Algorithm Validation

The box-counting algorithm that we developed is validated using a set of digitally modelled lightning discharge images in an environment protected by a vertical lightning rod. For this purpose, different positions (x) and heights (h) of the lightning rod were considered [37]. The fractal dimensions of such images were calculated using the expression (7) used by Djemai [58]. This expression is given by the following relation:

$$D_f = \frac{\ln(nb(i))}{\ln(lon(i))} \tag{7}$$

where nb(i) is the number of branches at the i-th step and lon(i) is the length of branches at the i-th step.

Figure 10 shows the shapes of simulated discharges for a lightning rod height of $h = 2$ cm and different values of the position x. The discharge shapes simulated by Khelil [37] were used to compare the fractal dimensions obtained by our box-counting algorithm with those calculated using Formula 7. This allows testing and validating the effectiveness of our algorithm.

Table 5 compiles the estimated fractal dimensions using formula 7 as well as those calculated by our algorithm, along with the errors between them, for various values the of positions (x) and heights (h) of the lightning rod. We found that the relative error between the fractal dimensions (FD_1) calculated by [37] using formula 7 and those (FD_2) calculated by our algorithm does not exceed 2.53%.

The box-counting algorithm that we have implemented is also examined based on a reference image whose fractal dimension is known in advance. For this purpose, the Fibonacci word

TABLE 5 | Comparison of the FDs calculated both by formula 6 and by our algorithm for different values of the positions (x) and heights (h) of the lightning rod.

h **(cm)**	***x*** **(cm)**	$\mathbf{FD_1}$	$\mathbf{FD_2}$	**Absolute error:** $\mathbf{\lvert FD_1 - FD_2 \rvert}$	**Relative error (%)**
0.2	0	1.1420	1.1493	0.0073	0.64
0.2	0.2	1.1590	1.1496	0.0094	0.81
0.2	0.37	1.1530	1.1329	0.0201	1.74
0.2	0.38	1.1420	1.1441	0.0021	0.18
0.2	0.38	1.1140	1.1102	0.0038	0.34
0.2	0.4	1.1300	1.1246	0.0054	0.48
0.2	0.4	1.1330	1.1409	0.0079	0.70
0.2	0.6	1.1250	1.1535	0.0285	2.53
0.2	1	1.1480	1.1636	0.0156	1.36
0.3	0	1.1620	1.1327	0.0293	2.52
0.3	0.2	1.1360	1.1220	0.0140	1.23
0.3	0.4	1.1500	1.1481	0.0019	0.16
0.3	0.6	1.1360	1.1403	0.0043	0.38
0.3	0.62	1.1360	1.1316	0.0044	0.39
0.3	0.63	1.1310	1.1352	0.0042	0.37
0.3	1	1.1420	1.1626	0.0206	1.80

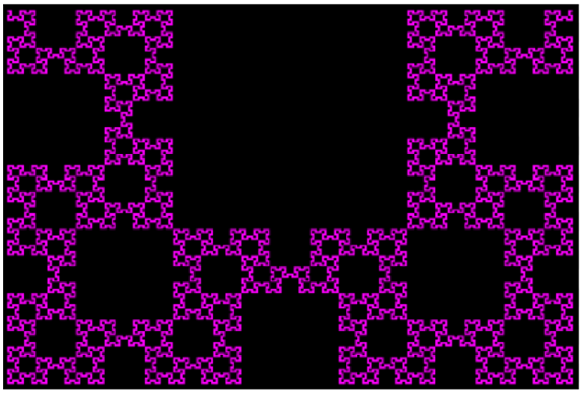

FIGURE 11 | Fractal curve of the Fibonacci word for $\alpha = 90°$.

fractal shown in Figure 11 is used as a means to test and validate the effectiveness of our algorithm. The image presented in Figure 11 is generated using an online Fibonacci word fractal generator (onlinemathtools.com). This tool generates fractals of the Fibonacci word, which is a self-similar plane curve generated from Fibonacci words. The length, height, and number of iterations of the fractal selected to validate our algorithm are 900 px, 600 px, and 20 iterations, respectively.

The Hausdorff dimension of the generalized Fibonacci fractal word for an angle α is defined by the relation [59]:

$$\mathrm{DF} = 3\,\frac{\log \emptyset}{\log\left(1+\cos\alpha+\sqrt{(1+\cos\alpha)^2+1}\right)} = 1,6379 \qquad (8)$$

where $\emptyset = \frac{1+\sqrt{5}}{2}$ and $\alpha = 90°$

The fractal dimension obtained by our proposed box-counting algorithm is equal to 1.6083, with an error of 2.96% compared to the theoretical dimension.

8 | Results and Discussion

In this section, we use fractal theory to diagnose the surface condition of a polluted insulator. Subsequently, the box-counting algorithm we implemented was adapted to calculate the fractal dimension of a set of discharge images. These images were extracted from videos recorded during pollution flashover tests on an experimental model.

The heatmap in Figure 12 illustrates the relationships between NSDD, Voltage, and FD. The colour coding provides an intuitive interpretation; cool colours represent lower FD values, while warm colours indicate higher values. This shows that NSDD has a dominant effect, significantly increasing FD as pollution levels rise, while applied voltage exerts a moderate influence, causing slight increases in FD. The gradient from lower to higher FD values highlights the combined impact of these factors, demonstrating that FD increases slightly with applied voltage and more substantially with NSDD.

We investigated the influence of applied voltage (ranging from 35 to 67 kV) and NSDD values (0.02, 0.03, and 0.04 g/cm^2) on the fractal dimensions of discharge images. The resulting fractal dimensions are presented in Figures 13 and 14.

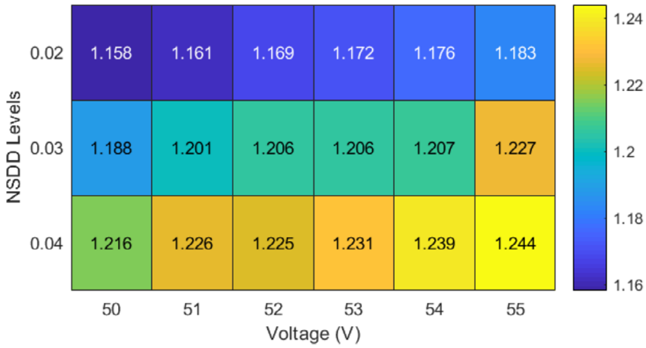

FIGURE 12 | Heatmap of FD values for different NSDD and applied voltage.

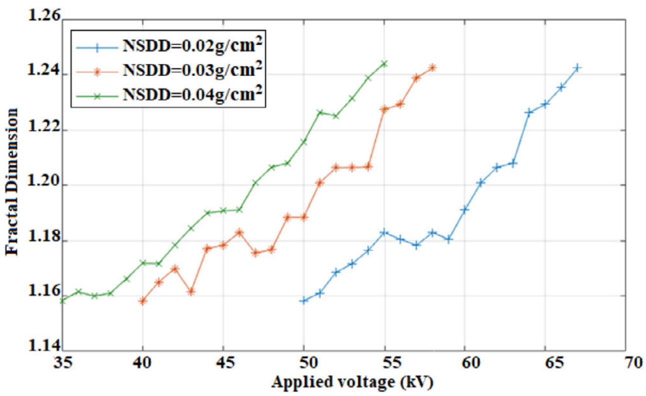

FIGURE 13 | Variation of fractal dimension in discharge images as function of applied voltage for different NSDD values.

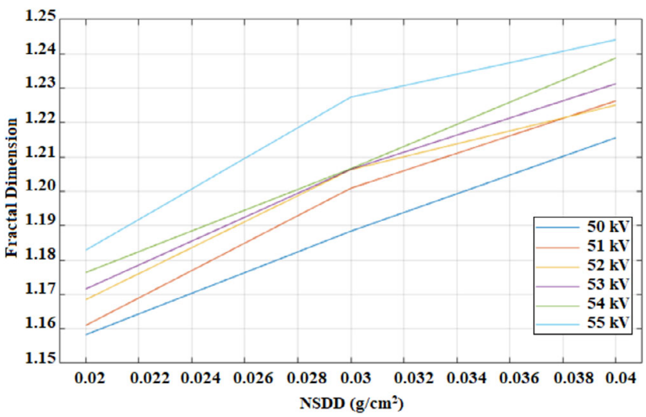

FIGURE 14 | Variation of the fractal dimension of discharge images with respect to NSDD for different applied voltage values.

8.1 | Study of the Fractal Dimension of Discharge Images as a Function of Applied Voltage

Figure 13 illustrates the variation of the fractal dimension (DF) in discharge images concerning the applied voltage, considering different values of NSDD. The results indicate that the fractal dimension of the discharge images generally falls within the range of 1 to 2. This is expected since our discharge evolves on a plane.

TABLE 6 | Discrimination between no-arc and arc discharges for NSDD 0.02, 0.03, and 0.04 g/cm^2.

NSDD (g/cm^2)	Range of applied voltage	FD	Type of discharge
0.02	50 to 60	€ [1,1583, 1,1910]	No-arc
	51 to 67	€ [1,2009, 1,2423]	Arc
0.03	40 to 50	€ [1,1586, 1,1917]	No-arc
	51 to 58	€ [1,2015, 1,2430]	Arc
0.04	35 to 46	€ [1,1588, 1,1920]	No-arc
	47 to 55	€ [1,2019, 1,2435]	Arc

According to this figure, we first observe that, for a given NSDD value, the fractal dimension (FD) increases non-linearly with the applied voltage. However, the FD increases rapidly for the lowest NSDD value (0.02 g/cm^2), where the discharges tend to occupy more space in the image, resulting in a significantly larger number of boxes.

For the highest NSDD value (0.04 g/cm^2), the fractal dimension (FD) increases less rapidly due to the gradual evaporation of the pollution layer. This evaporation is attributed to the increasing current density on the insulating surface, where water gradually evaporates as a result of Joule heating. This results in a slow evolution of the discharge space filling in the image. Consequently, the FD increases gradually and progressively. Experimental observations indicate that flashover can occur when the FD approaches the value of 1.24. At this maximum FD value, the discharges in the image appear dense and their filling is nearly complete (Figure 5g).

The fluctuations observed at the beginning of each graph are due to the fact that, during the initial stages of the flashover phenomenon, the discharges appear as scattered and dispersed points (Figure 5a,b,c), which appear and disappear rapidly until some of them join to form arc structures. The presence of these arcs tends to attenuate or even eliminate the fluctuations, as the arcs dominate the image compared to small bright spots. Therefore, as shown in Table 6, we propose the discrimination between two main types of discharges: arc-type discharges and no-arc type discharges, based on the calculated fractal dimensions.

Based on the discrimination presented in the previous table, we have concluded that we can detect the presence of arc type electrical discharges from recorded images by calculating their fractal dimensions (FD). Thus, if the FD of the discharge image is strictly less than 1.2, the discharge is of the 'no-arc' type. Conversely, if it is greater than this value, the discharge is of the 'arc' type.

The distinction between "arc" and "no-arc" discharges offers a non-invasive monitoring tool for insulators. This approach can be integrated into automated systems, enabling early detection of dangerous discharges, optimizing maintenance schedules, and reducing costs by intervening only when the fractal dimension (FD) reaches a critical threshold. It is particularly useful for remote monitoring, especially in hard-to-access areas, and could contribute to the development of safety standards based on FD for more effective management of risks associated with insulator pollution.

8.2 | Study of the Fractal Dimension of Discharge Images as a Function of NSDD

Figure 14 depicts the evolution of the fractal dimension (FD) of discharge images as a function of NSDD for different applied voltages ranged from 50 kV to 55 kV.

According to Figure 14, we observe that the fractal dimension (DF) increases non-linearly with the value of the NSDD for each applied voltage. Such variation indicates an increase in discharge activity on the surface of the insulator, which is reflected in a denser filling of the discharges in the image. For all applied voltage values, it is observed that the increase in FD slows down (in the order of 0.021) between the highest NSDD values, namely 0.03 and 0.04 g/cm^2. Thus, we observe that the variation in FD from the lowest NSDD (0.02 g/cm^2) to the value (0.03 g/cm^2) is relatively significant (in the order of 0.039). Therefore, FD quantifies the evolution of NSDD in a remarkable way.

The correlation between fractal dimension (FD) and NSDD offers valuable insights for real-time monitoring of insulator pollution levels without the need for invasive methods or direct measurements. This approach allows pollution levels to be estimated from images of energized insulators, providing early warning to maintenance teams before critical thresholds are reached. By incorporating FD calculations into monitoring systems, cleaning or replacement actions can be planned more effectively based on actual data, reducing maintenance costs and extending the lifespan of insulators by intervening only when FD indicates dangerous levels of pollution. These findings contribute to the development of standards for assessing the safety of insulators in polluted environments and optimizing interventions. However, it is important to acknowledge some limitations, such as the reliance on image quality and the need for further validation in diverse different field conditions. Future research could explore the integration of additional variables, such as environmental factors, to enhance the accuracy of pollution assessments and improve the robustness of the monitoring system. This non-invasive, data-driven approach based on FD represents a valuable tool for improving insulator management and maintenance practices, contributing to safer and more efficient electrical systems.

8.3 | Practical Implementation Considerations

We acknowledge the importance of addressing the practical implementation of the proposed methodology in real-world scenarios. To integrate this approach into existing monitoring systems, several hardware and software components are required. High-resolution cameras that are capable of capturing discharge activity on insulators under varying lighting and environmental conditions form the foundational hardware requirement. For real-time processing, edge computing devices such as NVIDIA Jetson modules can be employed to run the fractal dimension calculation algorithm. On the software side, platforms such as MATLAB or Python, combined with image processing libraries like OpenCV, facilitate the analysis and computation of fractal dimensions. While the proposed method offers cost-effective monitoring through the use of non-invasive techniques, initial investments in hardware, software licensing, and system calibration must be considered. Despite these initial costs, the long-term benefits, including reduced maintenance costs, early hazard detection, and enhanced system reliability, justify the implementation of this approach in industrial settings. Future work could explore streamlining the algorithm for integration into fully automated monitoring systems.

8.4 | Broader Implications and Future Directions

While the proposed methodology focuses on the analysis of discharge activity in contaminated insulator models, it has broader implications. For instance, the fractal geometry approach could be adapted to diagnose other materials or systems where surface irregularities affect performance, such as in corrosion detection or quality control in manufacturing. In addition, this work lays the groundwork for extending fractal-based diagnostic methods to insulators exposed to varied environmental conditions and to different types of electrical equipment. Future research could explore the integration of machine learning techniques to enhance classification accuracy and scalability. Thus, this study not only advances the understanding of discharge phenomena but also opens new avenues for interdisciplinary applications and innovations in diagnostic technologies.

9 | Conclusion

This paper presents a novel methodology for analysing discharge activity and monitoring flashovers in uniformly polluted insulator models, leveraging fractal geometry to characterize discharge images. The proposed algorithm calculates the fractal dimension (FD) of discharge images using the box-counting method. The approach involves binarizing RGB images with the Niblack method, transforming matrices into square matrices, and calculating FDs over multiple resolutions.

The algorithm was validated by comparing its results to established benchmarks, showing a maximum relative error below 3%. Applied to discharge images, the FD values ranged from 1.15 to 1.25, increasing with applied voltage and non-soluble deposit density (NSDD). Notably, discharges were classified as "no-arc" for FD values below 1.2 and "arc" otherwise, demonstrating the reliability of FD as a diagnostic metric.

This study confirms that fractal analysis of discharge images offers a non-invasive, real-time method for monitoring insulator pollution levels. By correlating FD with NSDD, this approach facilitates early hazard detection, reduces maintenance costs, and supports informed decision-making for cleaning or replacement actions. However, certain limitations of the proposed method should be acknowledged. The accuracy of FD calculations can be affected by image quality, with noise or low resolution potentially affecting the binarization process and FD estimation. In addition, varying lighting conditions might impact the visibility of discharge features, emphasizing the need for validation under different lighting scenarios. Furthermore, calibration is essential when applying the method to different types of insulators or environmental conditions to ensure its robustness. These findings contribute to developing safety standards and optimize maintenance strategies, particularly in remote or challenging environments. Furthermore, integrating this method into existing monitoring systems requires high-resolution cameras, edge computing devices, and image processing platforms, which, despite their initial cost, offer significant long-term benefits.

These findings not only contribute to improve maintenance strategies for electrical insulators but also open the door to broader applications of fractal geometry in diagnostics and monitoring in various fields, inspiring future research and practical advances.

Author Contributions

Imene Ferrah: formal analysis, investigation, methodology, writing – original draft. **Youcef Benmahamed:** methodology, supervision, validation, writing – original draft. **Hayder K. Jahanger:** analysis, resources, visualization, writing – review & editing. **Madjid Teguar:** supervision, validation, revision. **Omar Kherif:** formal analysis, software.

Conflicts of Interest

The authors declare no conflicts of interest.

Data Availability Statement

The data that support the findings of this study are available from the corresponding author upon reasonable request.

References

1. A. K. Chaou, A. Mekhaldi, and M. Teguar, "Elaboration of Novel Image Processing Algorithm for Arcing Discharges Recognition on HV Polluted Insulator Model," *IEEE Transactions on Dielectrics and Electrical Insulation* 22, no. 2 (2015): 990–999.

2. A. K. Chaou, A. Mekhaldi, and M. Teguar, "Recurrence Quantification Analysis as a Novel LC Feature Extraction Technique for the Classification of Pollution Severity on HV Insulator Model," *IEEE Transactions on Dielectrics and Electrical Insulation* 22, no. 6 (2015): 3376–3384.

3. N. Dhahbi and A. Beroual, "Time–frequency Analyses of Leakage Current Waveforms of High Voltage Insulators in Uniform and Non-uniform Polluted Conditions," *IET Sci, Meas Technol* 9, no. 8 (2015): 945–954.

4. L. Jin, D. Ma, Z. Yuan, G. Zhou, and S. Han, "Evaluation of Surface Discharge of Polluted Insulator Based on Optical Emission Spectroscopy Measurements," *IEEE Transactions on Dielectrics and Electrical Insulation* 31, no. 1 (2024): 350–357.

5. B. X. Du, Y. Liu, H. J. Liu, and Y. J. Yang, "Recurrent Plot Analysis of Leakage Current for Monitoring Outdoor Insulator Performance," *IEEE Transactions on Dielectrics and Electrical Insulation* 16, no. 1 (2009): 139–146.

6. A. K. Chaou, A. Mekhaldi, B. Moula, et al., "The Use of Wavelets for the Monitoring and Diagnostic of Surface state of HV Polluted Insulators," in *IEEE International Conference on Electrical Sciences and Technologies in Maghreb* (IEEE, 2014), 1–8

7. H. de Santos and M. Á. Sanz-Bobi, "A Machine Learning Approach for Condition Monitoring of High Voltage Insulators in Polluted Environments," *Electric Power Syst Res* 220 (2023): 109340.

8. Y. Liu and B. X. Du, "Recurrent Plot Analysis of Leakage Current on Flashover Performance of Rime-iced Composite Insulator," *IEEE Transactions on Dielectrics and Electrical Insulation* 17, no. 2 (2010): 465–472.

9. X. Jiang, Y. Shi, C. Sun, and Z. Zhang, "Evaluating the Safety Condition of Porcelain Insulators by the Time and Frequency Characteristics of LC Based on Artificial Pollution Tests," *IEEE Transactions on Dielectrics and Electrical Insulation* 17, no. 2 (2010): 481–489.

10. D. Pylarinos, S. Lazarou, G. Marmidis, and E. Pyrgioti, "Classification of Surface Condition of Polymer Coated Insulators Using Wavelet Transform and Neural Networks," in *International Conference on Wavelet Analysis and Pattern Recognition*, (IEEE, 2007), 658–663.

11. L. Liu, H. Mei, C. Guo, Y. Tu, and L. Wang, "Pixel-level Classification of Pollution Severity on Insulators Using Photothermal Radiometry and Multiclass Semisupervised Support Vector Machine," *IEEE Trans Ind Informat* 17, no. 1 (2021): 441–449.

12. I. Ferrah, A. K. Chaou, D. Maadjoudj, and M. Teguar, "Novel Colour Image Encoding System Combined With ANN for Discharges Pattern Recognition on Polluted Insulator Model," *IET Sci, Meas Technol* 14, no. 6 (2020): 718–725.

13. A. K. Chaou, A. Mekhaldi, and M. Teguar, "Recurrence Quantification Analysis as a Novel LC Feature Extraction Technique for the Classification of Pollution Severity on HV Insulator Model," *IEEE Transactions on Dielectrics and Electrical Insulation* 22, no. 6 (2015): 3376–3384.

14. N. Al khafaf and A. H. El-Hag, "Prediction of Leakage Current Peak Value," in *International Symposium on Mechatronics and Its Applications (ISMA 2018)*, (IEEE, 2018), 1–4

15. A. A. Salem, K. Y. Lau, Z. Abdul-Malek, et al., "Polymeric Insulator Conditions Estimation by Using Leakage Current Characteristics Based on Simulation and Experimental Investigation," *Polymers* 14, no. 4 (2022): 737.

16. A. A. Salem, R. Abd-Rahman, S. A. Al-Gailani, et al., "Risk Assessment of Polluted Glass Insulator Using Leakage Current Index Under Different Operating Conditions," *IEEE Access* 8 (2020): 175827–175839.

17. O. E. Gouda, M. M. F. Darwish, K. Mahmoud, M. Lehtonen, and T. M. Elkhodragy, "Pollution Severity Monitoring of High Voltage Transmission Line Insulators Using Wireless Device Based on Leakage Current Bursts," *IEEE Access* 10 (2022): 53713–53723.

18. R. Shariatinasab, S. Saghafi, M. Khorashadizadeh, and M. Ghayedi, "Probabilistic Assessment of Insulator Failure Under Contaminated Conditions," *IET Sci, Meas Technol* 14, no. 5 (2020): 557–563.

19. W. Chen, W. Wang, Q. Xia, B. Luo, and L. Li, "Insulator Contamination Forecasting Based on Fractal Analysis of Leakage Current," *Energies* 5, no. 7 (2012): 2594–2607.

20. A. Hui and R. Lv, "The Fractal of Insulator Leakage Current With the Tunable Q-factor Wavelet Transform," in *2020 7th International Forum on Electrical Engineering and Automation (IFEEA)* (IEEE, 2020), 281–284

21. A. Hui, J. Zheng, H. Lin, and B. He, "Wavelet-fractal Characteristics of Leakage Current on HV Insulators," in *2008 Third International Conference on Electric Utility Deregulation and Restructuring and Power Technologies* (IEEE, 2008), 732–736

22. J. Song, B. Wang, Q. Jiang, and X. Hao, "Exploring the Role of Fractal Geometry in Engineering Image Processing Based on Similarity and Symmetry: A Review," *Symmetry* 16, no. 12 (2024): 1658.

23. B. B. Mandelbrot, *The Fractal Geometry of Nature*, 1st ed. (WH Freeman, 1982).

24. Y. Q. Li, "Generalized Koch Curves and Thue–Morse Sequences," *Fractals* 29, no. 6 (2021): 2150130.

25. D. Khelil, S. Bouazabia, D. Maadjoudj, and P. N. Mikropoulos, "A Fractal Model of Discharge Interception Probability of a Vertical Grounded Rod in the Presence of a Neighboring Object," *Journal of Electrostatics* 95 (2018): 42–52.

26. D. Amarasinghe, U. Sonnadara, M. Berg, and V. Cooray, "Fractal Dimension of Long Electrical Discharges," *Journal of Electrostatics* 73 (2015): 33–37.

27. M. Yu, L. Xing, L. Wang, F. Zhang, X. Xing, and C. Li, "An Improved Multifractal Detrended Fluctuation Analysis Method for Estimating the Dynamic Complexity of Electrical Conductivity of karst Springs," *Journal of Hydroinformatics* 25, no. 2 (2023): 174–190.

28. A. Mukhopadhyay, T. K. Barman, P. Sahoo, and J. P. Davim, "Modeling and Optimization of Fractal Dimension in Wire Electrical Discharge Machining of EN 31 Steel Using the ANN-GA Approach," *Materials* 12, no. 3 (2019): 454.

29. W. Feng, X. Chu, Y. Hong, and D. Deng, "Surface Morphology Analysis Using Fractal Theory in Micro Electrical Discharge Machining," *Materials Transactions* 58, no. 3 (2017): 433–441.

30. Y. Sawada, S. Ohta, M. Yamazaki, and H. Honjo, "Self Similarity and a Phase Transition-Like Behavior of a Random Growing Structure Governed by a Non-equilibrium Parameter," *Physical Review A* 26 (1982): 3557–3563.

31. L. Niemeyer, L. Pietronero, and H. J. Wiesmann, "Fractal Dimension of Dielectric Breakdown," *Physical Review Letter* 52 (1984): 1033–1036.

32. H. J. Wiesmann and H. R. Zeller, "A Fractal Model of Dielectric Breakdown and Prebreakdown in Solid Dielectrics," *Journal of Applied Physics* 60 (1986): 1770–1773.

33. N. I. Pertov, N. G. Petrova, and F. D'Alessandro, "Quantification of the Probability of Lightning Strikes to Structures Using a Fractal Approach," *IEEE Transactions on Dielectrics and Electrical Insulation* 10, no. 4 (2003): 641–654.

34. M. D. N. Perera and D. U. J. Sonnadara, "Fractal Nature of Simulated Lightning Channels," *Sri Lankan Journal of Physics* 13, no. 2 (2013): 09–25.

35. D. Khelil, S. Bouazabia, and P. N. Mikropoulos, "Measurement and Approximation by Simulation of the Instantaneous Breakdown Voltage of Lightning Discharge in the Presence of Protection," *COMPEL—The International Journal for Computation and Mathematics in Electrical and Electronic Engineering* 41, no. 4 (2022): 1159–1170.

36. M. Molas and M. Szewczyk, "Parameters of 3D Fractal Dimension for a Population of Long Spark Discharges," *IEEE Transactions on Power Delivery* 39, no. 1 (2024): 296–305.

37. D. Khelil, "Modélisation de la Décharge De Foudre En Présence d'un Paratonnerre et Détermination de Sa Dimension Fractale" (master's thesis, Algiers, 2008), https://repository.enp.edu.dz/jspui/bitstream/123456789/5970/1/KHELIL.Djazia.pdf

38. D. Maadjoudj, A. Mekhaldi, and M. Teguar, "Flashover Process and Leakage Current Characteristics of Insulator Model Under Desert Pollution," *IEEE Transactions on Dielectrics and Electrical Insulation* 25, no. 6 (2018): 2296–2304.

39. S. Heddam, "Multi-layer Perceptron Neural Network-based Approach for Modelling Phycocyanin Pigment Concentrations: Case Study From lower Charles river Buoy, USA," *Environmental Science and Pollution Research* 23, no. 17 (2016): 17210–17225.

40. S. Greenland, S. J. Senn, K. J. Rothman, et al., "Statistical Tests, P Values, Confidence Intervals, and Power: A Guide to Misinterpretations," *European Journal of Epidemiology* 31, no. 4 (2016): 337–350.

41. D. C. Montgomery, E. A. Peck, and G. G. Vining, *Introduction to Linear Regression Analysis* (John Wiley & Sons, 2021).

42. D. C. Montgomery, *Design and Analysis of Experiments*, 9th ed. (John Wiley & Sons, 2017).

43. D. S. Moore, G. P. McCabe, L. C. Alwan, and B. A. Craig, *The Practice of Statistics for Business and Economics* (WH Freeman and Company, 2016).

44. A. Burambekova and P. Shamoi, "Comparative analysis of color models for human perception and visual color difference," arXiv preprint, arXiv:2406.19520, 2024

45. K. K. D. Ramesh, G. K. Kumar, K. Swapna, D. Datta, and S. S. Rajest, "A Review of Medical Image Segmentation Algorithms," *EAI Endorsed Trans Pervasive Health Technol* 7, no. 27 (2021): e6.

46. S. Bhowmik, "Document Image Binarization," *Document Layout Analysis* (Springer Nature, 2023), 11–30.

47. N. Otsu, "A Threshold Selection Method From Gray-level Histograms," *IEEE Transactions on Systems, Man, and Cybernetics* 9, no. 1 (1979): 62–66.

48. S. Saha, M. A. Rahman, and A. Thakur, "Design and Implementation of SPI Bus Protocol With Built-in-self-test Capability Over FPGA," in *International Conference on IEEE Electrical Engineering and Information & Communication Technology* (IEEE, 2014), 1–6

49. F. L. Gaol and T. Taxt, "Bresenham Algorithm: Implementation and Analysis in Raster Shape," *Journal of Computers* 8, no. 1 (2013): 69–78.

50. K. Khurshid, I. Siddiqi, and C. Faure, "Comparison of Niblack Inspired Binarization Methods for Ancient Documents," *SPIE In Document Recognition and Retrieval XVI* 7247 (2009): 267–275.

51. A. Tsao, P. Nardelli, A. B. Waxman, R. San José Estépar, G. R. Washko, and F. N. Rahaghi, "Fractal Dimension Estimation Using Box Counting Method to Quantify CT-based Pulmonary Vascular Tree Simplification," in *D106. NOE Valley: Clots, COVID, and Lung Vascular Diseases* (American Thoracic Society, 2022), A5436–A5436

52. Q. Fu, C. Li, F. Cai, W. Wang, and S. Xiao, "Emitter Signal Sorting Based on Fractal Dimensions of Pulse Envelope's front Edge," in *International Conference on Military Communications and Information Systems (ICMCIS)* (IEEE, 2016), 1–5

53. J. Li, Q. Du, and C. Sun, "An Improved Box-counting Method for Image Fractal Dimension Estimation," *Pattern Recognition* 42, no. 11 (2009): 2460–2469.

54. N. Rajković, B. Krstonošić, and N. Milošević, "Box-counting Method of 2D Neuronal Image: Method Modification and Quantitative Analysis Demonstrated on Images From the Monkey and human Brain," *Computational and Mathematical Methods in Medicine* 2017 (2017): 8967902.

55. A. Di Ieva, F. J. Esteban, F. Grizzi, and W. Klonowski, "Fractals in the Neurosciences, Part II: Clinical Applications and Future Perspectives," *The Neuroscientist* 21, no. 1 (2015): 30–43.

56. N. T. Miloevic, "Fractal Analysis of Two Dimensional Images: Parameters of the Space-filling and Shape," in *International Conference on Control Systems and Computer Science* (IEEE, 2014), 539–544

57. T. Wen and K. H. Cheong, "The Fractal Dimension of Complex Networks: A Review," *Information Fusion* 73 (2021): 87–102.

58. Z. Djemai and A. Beroual, "Fractal Dimension of Discharges Propagation on Insulating Interfaces," *Archives of Electrical Engineering* 47, no. 3 (1998): 251–256.

59. A. Monnerot-Dumaine, *The Fibonacci Word Fractal* (HAL, 2009).